# Data-Guided Discovery of Ocean Dynamics

**Qi-fan Wu**
Niels Bohr Institute
University of Copenhagen
qifan.wu@nbi.ku.dk

**Dion Häfner**
Pasteur Labs
dion.haefner@simulation.science

**Roman Nuterman**
Niels Bohr Institute
University of Copenhagen
nuterman@nbi.ku.dk

**Guido Vettoretti**
Department of Physical and Environmental Sciences
University of Toronto
g.vettoretti@utoronto.ca

**Markus Jochum**
Niels Bohr Institute
University of Copenhagen
mjochum@nbi.ku.dk

## Abstract

From paleoclimate records we know that during the last 100,000 years parts of the North Atlantic ocean circulation have collapsed and recovered frequently. Only recently has the climate community been able to reproduce these Dansgaard-Oeschger events with numerical simulations of Earth System Models. However, simulations are computationally expensive and since an analytical framework for this circulation is missing, it is not yet clear what causes recovery or collapses. Here, we use sparse regression framework to build a set of stochastic differential equations that emulate the Earth System Models' behavior and use it to show that collapses are deterministic, but recoveries are stochastically forced.

## 1 Introduction

The Atlantic Meridional Overturning Circulation (AMOC) is a system of ocean currents that plays a key role in Earth's climate in the past and present [1]. Greenland ice core records provide evidence for Dansgaard–Oeschger (D–O) events that are characterized by abrupt warming into warm interstadial periods followed by gradual cooling into cold stadial periods [2], and Community Earth System Model (CESM) simulations suggest that these dramatic climate change events were linked to sudden transitions in the AMOC [3]. There is no analytical framework for the AMOC, and although there are various hypotheses about the mechanisms that drive AMOC changes, a unifying theory that fully explains them is still lacking [4]. Thus, we explored data-driven tools to derive a set of interpretable coupled differential equations that are computationally efficient to emulate the AMOC, and hopefully allow for a dynamical interpretation.

A previous parsimony analysis of CESM simulations identifies surface freshwater flux (SFWF), potential density at 200 meters (PD_200m, both averaged between $50°\mathrm{N}$ and $70°\mathrm{N}$) and AMOC strength (the maximum at $40°\mathrm{N}$) as the simplest coupled set of controlling variables (published by the present authors). In the present work, we use the time series data of these three key variables as input, employ sparse regression with a polynomial dependency structure, similar in spirit to symbolic regression approaches such as Sparse Identification of Nonlinear Dynamical systems (SINDy) [5], and apply regularization to control complexity. We obtain a discrete-time dynamical system with

1st Workshop on Differentiable Systems and Scientific Machine Learning @ EurIPS 2025.

three stochastic differential equations that can be used to test hypotheses about the cause of AMOC transitions. Below we discuss the various steps and decisions that lead to the final set of equations.

## 2 Methods

This work uses the annual time series of three key variables (SFWF, PD_200m, and AMOC) from four 8000-year long CESM simulations with glacial boundary conditions that reproduce the observed structure of D–O events [6, 7]. The time series to be studied in this work have several important features, including irregular transitions and a low signal-to-noise ratio. We note that the system's evolution is strongly influenced by stochastic variability through drift–diffusion estimation [8–12] (Appendix A.1, Figure A.1). By constructing a polynomial dependency structure up to the fourth order, symbolic regression builds candidate functions for key variables and their nonlinear interactions, with added random noise to perturb the system for simulation [13–17]. Sparse regression is then applied using an $\ell_1$-regularized (lasso) formulation that performs variable selection and coefficient shrinkage, balancing model accuracy with simplicity and thereby controlling equation complexity [18, 19]. The data-driven discrete-time stochastic differential equation (SDE) model can be written as

$$\begin{aligned} \mathrm{AMOC}_{t+1} &= f(\mathrm{AMOC}_t, \mathrm{PD}_t, \mathrm{SFWF}_t) + \epsilon_{\mathrm{AMOC}}, \\ \mathrm{PD}_{t+1} &= g(\mathrm{AMOC}_t, \mathrm{PD}_t, \mathrm{SFWF}_t) + \epsilon_{\mathrm{PD}}, \\ \mathrm{SFWF}_{t+1} &= h(\mathrm{AMOC}_t, \mathrm{PD}_t, \mathrm{SFWF}_t) + \epsilon_{\mathrm{SFWF}}. \end{aligned} \tag{1}$$

with $f, g, h$ being learned via symbolic regression, and $\epsilon$ representing normally distributed Gaussian noise whose range is defined by these residuals. It should be mentioned that for this specific problem, the SINDy method which assumes deterministic dynamics and is computationally expensive, did not perform well [5].

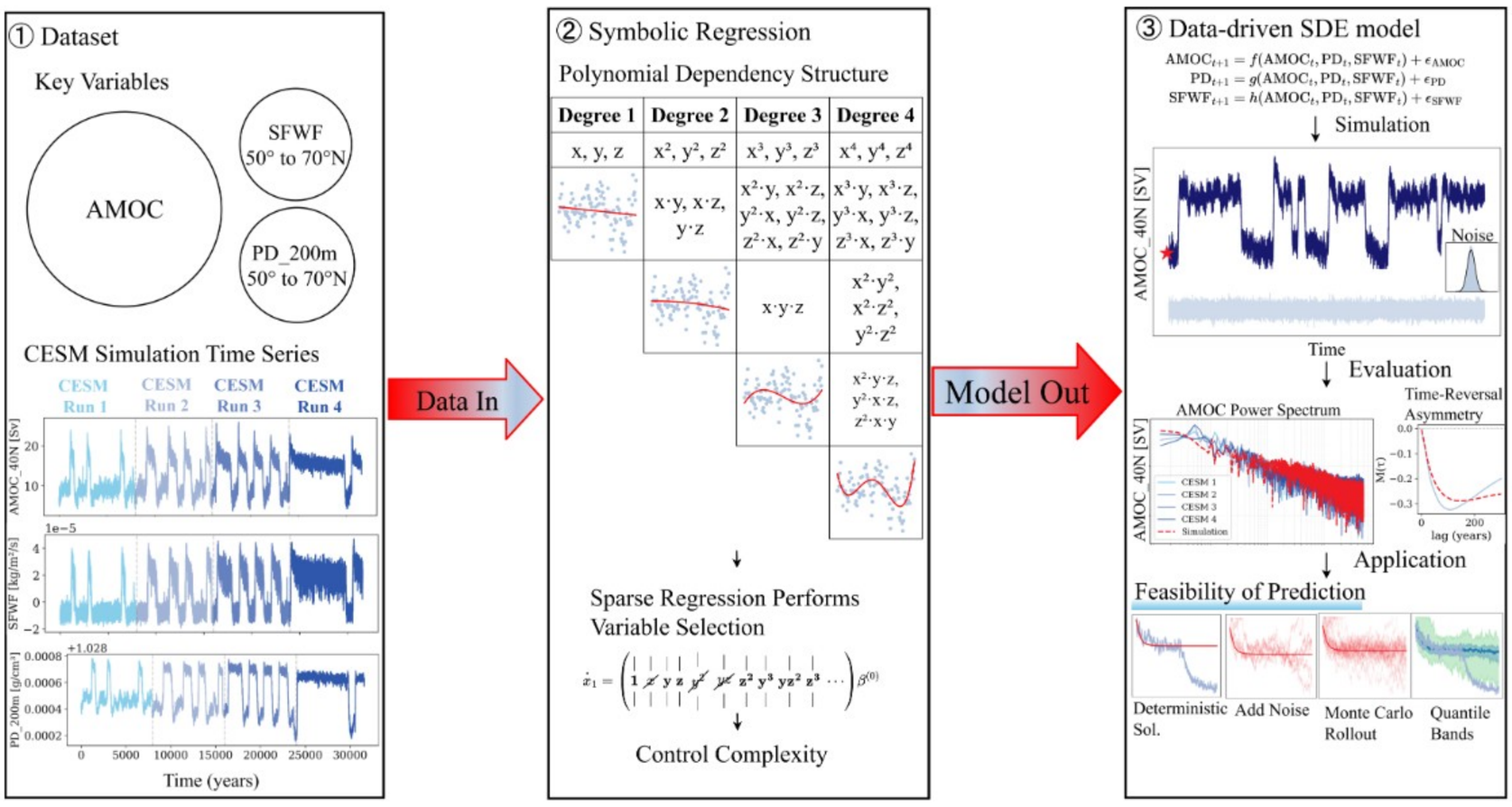


Figure 1: Schematic of the basic workflow. Time series of AMOC, PD_200m, and SFWF from four CESM simulation runs serve as inputs ① to an equation discovery framework ②. The resulting data-driven SDE model simulates system evolution from an initial value marked by a red star and is evaluated using spectral and asymmetry metrics, enabling applications in climate prediction and analyses of system characteristics.

This set of equations reproduce the CESM fields, as demonstrated by a comparison of power spectra and time-reversal asymmetry [20–22]. These simulations are further extended using large ensembles to obtain a distribution of possible outcomes under stochastic forcing, enabling the feasibility of theoretical prediction tests and analyses of dynamical stability and attractor basins [23, 24]. Both Gaussian and empirically derived noise terms $\epsilon$ are assessed to evaluate the system's response to stochastic perturbations, with values randomly sampled from residual-based distributions defining

the noise range. This basic workflow is illustrated in Fig. 1. All experiments were run in an online Jupyter Notebook environment (Intel Xeon 2.20 GHz CPU × 2 cores, 13.6 GB RAM, no GPU). Each polynomial regression model required approximately 1 minute, and the full analysis workflow is completed in under 15 minutes, making it computationally efficient relative to the numerically intensive and computationally demanding CESM simulations [25], which need approximately 160 cores for a throughput of 100 year/day - or 3 months for a 10,000 year simulation.

## 3 Results

Our model successfully obtains bounded continuous solutions of Eq. (1) and emulates the co-evolution of the coupled variables. Using only the initial values, it reproduces the sudden transitions observed in CESM simulations and proxy records (Fig. 2a). As shown in Appendix A.2, the polynomial model of degree 4 with 30-year smoothing applied to the input data and perturbed with Gaussian noise best reproduces the transition dynamics. Compared with the SDE model derived from intuition based on a stochastic FitzHugh–Nagumo–type system with physics-motivated nonlinearities [6, 7], our data-driven model learned directly from CESM outputs better reproduces the realistic D–O events (Fig. 2b), with the cold stadial and warm interstadial phases and the sudden transitions between them (Tables A.1–A.3). Note that when the stochastic forcing amplitude is increased in the conceptual model of [6], the bimodality of the AMOC distribution tends to vanish, whereas our model preserves distinct states.

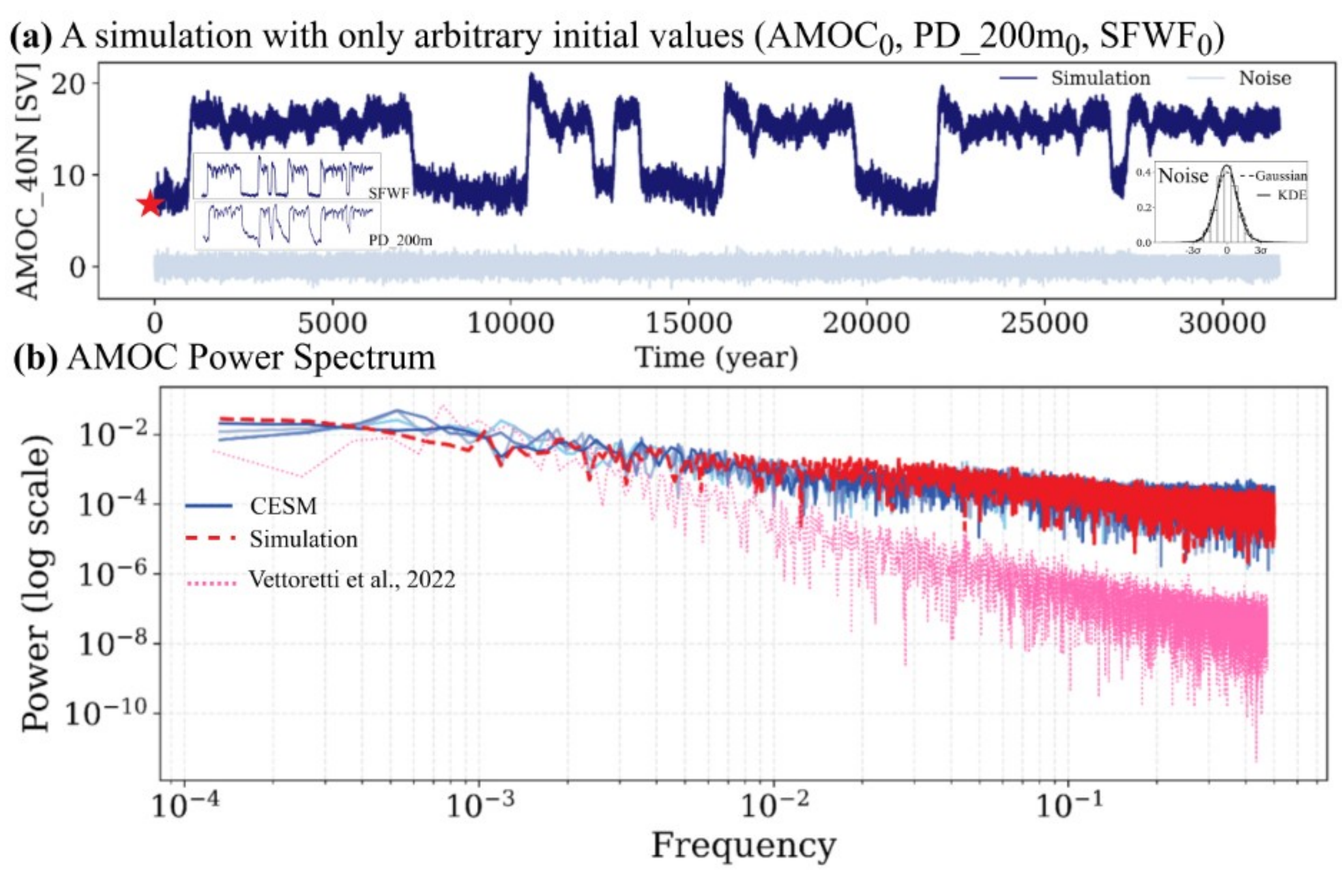


Figure 2: (a) Our model simulation initialized with only the initial values (red star) and driven by normally distributed Gaussian noise. The inset on the left shows the co-evolution of SFWF and PD_200m, while the inset on the right displays the noise distribution obtained from the residuals of the polynomial fits. (b) Power spectra of AMOC from CESM simulations, our model simulation, and the SDE model of [6].

We now take this SDE model as emulator of the AMOC in CESM, and study its sensitivity to noise, i.e., variability of climate on time scales smaller than 30 years like El Niño or the North Atlantic Oscillation [26]. The results show that the model is sensitive to initial conditions (Fig. 3a). As a concrete example, we demonstrate that the deterministic solutions (i.e., model evolution without noise perturbations) fails to reproduce off-on transitions, but can capture on-off transitions, whereas when perturbed with normally distributed noise, cold-to-warm transitions become possible and the simulated AMOC can reach the strength characteristic of the alternate state (Fig. 3a). We perform Monte Carlo rollouts (ensemble size $N = 50$) by integrating the stochastic system with independently sampled perturbations $\epsilon_{\text{AMOC}}, \epsilon_{\text{PD}}, \epsilon_{\text{SFWF}}$, generating an ensemble of trajectories that approximate the posterior distribution of system states, from which quantile bands (50% and 95%) are computed to quantify the range of possible outcomes under noise (Fig. 3a). We perform prediction tests using

deterministic and noisy simulations to evaluate the probability of correctly predicting AMOC states 50 years ahead across different dynamical regimes, showing that D–O events are primarily noise-driven rather than purely internally oscillatory (Fig. 3b). We now turn to the fixed-point and attractor basin analysis, where the deterministic part from the data-driven equations (Eq. (1)) is iteratively solved to identify equilibrium states and visualize their local stability structure in 3D phase space [23]; stochastic and deterministic trajectories are compared, showing that while the deterministic system remains confined near stable equilibria, stochastic perturbations enable transitions between coexisting AMOC states, reflecting the presence of multiple attractor basins in the system's phase space (Fig. 3c).

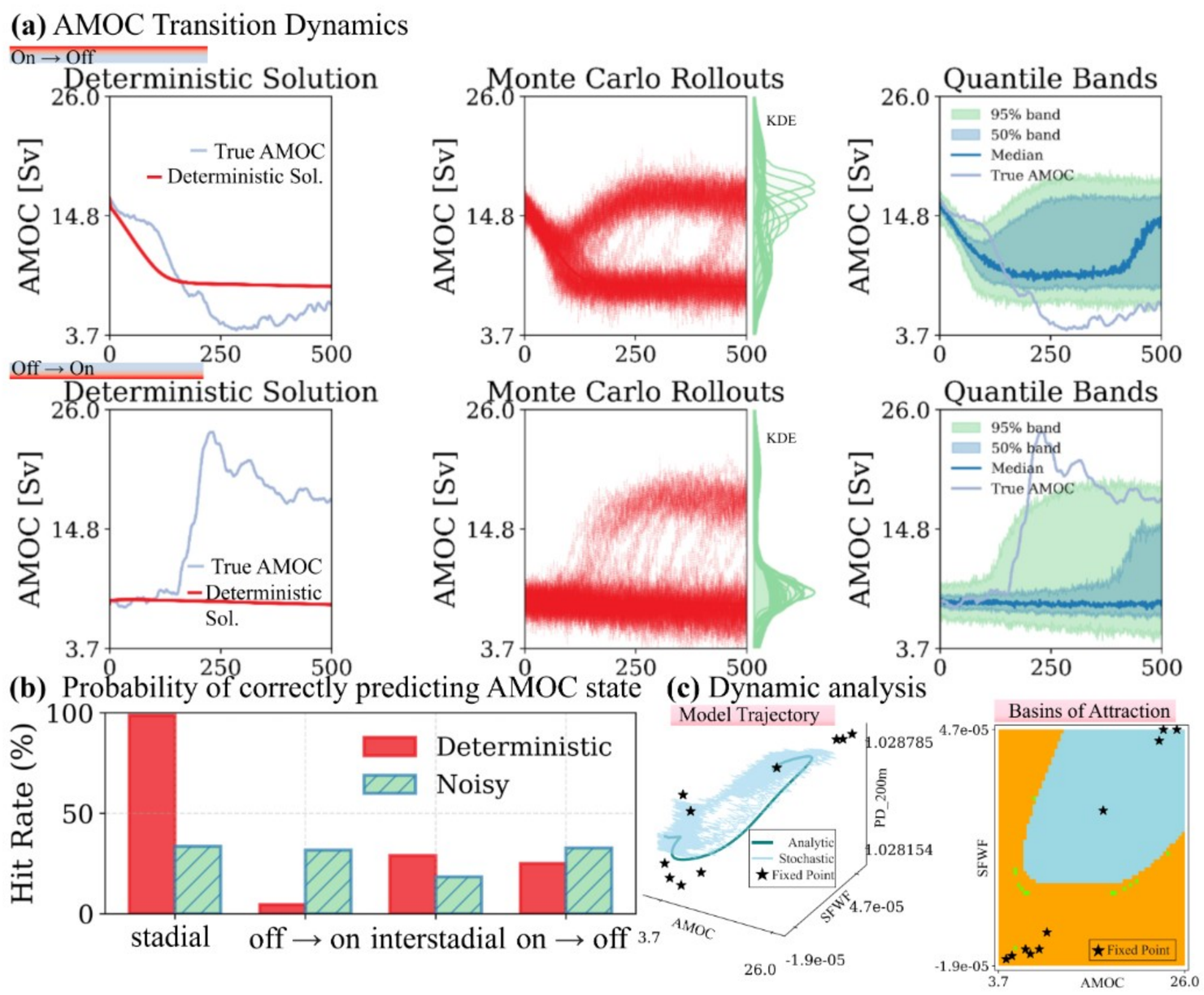


Figure 3: (a) Warm-to-cold and OFF/ON AMOC transitions are simulated using deterministic and stochastic models, where the deterministic solution, Monte Carlo rollouts, and quantile bands show the deterministic behavior, ensemble spread, and uncertainty. (b) The probability of correctly predicting AMOC states (stadial, interstadial, and transitions) for deterministic and noisy simulations indicates noise-driven transitions, especially during cold-to-warm phases. (c) Dynamic analysis of model trajectories and fixed points in the AMOC–SFWF–PD phase space, with corresponding basins of attraction.

## 4 Summary and discussion

We use a 32,000-year-long record of CESM simulations to learn a set of 3 SDEs that describe the AMOC behaviour, in particular its sudden transitions between on and off states. This set is computationally efficient so that it allows to study the importance of high-frequency variability, or noise, on the transitions. It also has much more realistic statistical properties than the simple sets of SDEs that are typically used for these problems (i.e., van-deer Pole or FitzHugh-Nagumo oscillators). We find that for the noise levels found in CESM, the off-on transitions require stochastic forcing [26], whereas on-off transitions are deterministic as proposed by [3]. Current and future work will explore how to further improve the quality of our SDEs with better data processing techniques and more sophisticated evaluation metrics. Moreover, we need to explore how robust the present results are to variations in structure and magnitude off the noise. We will then have a tool to explore the potential of the AMOC to undergo rapid transitions in the future.

## Acknowledgments and Disclosure of Funding

This research was funded through the Danish Research Fund project MAchine & Data Guided discovery of Ocean Dynamics (MADGOD) and the EU-Horizon project ClimTip (nr. 101137601). We are grateful for the computing resources provided by ther Danish Center of Climate Computing ($DC^3$).

## References

[1] T. Kuhlbrodt, A. Griesel, M. Montoya, A. Levermann, M. Hofmann, and S. Rahmstorf. On the driving processes of the atlantic meridional overturning circulation. *Reviews of Geophysics*, 45 (2), 2007. doi: 10.1029/2004RG000166.

[2] W. Dansgaard, S. Johnsen, H. Clausen, D. Dahl-Jensen, N. Gundestrup, C. Hammer, C. Hvidberg, J. Steffensen, A. Sveinbjornsdottir, J. Jouzel, and G. Bond. Evidence for general instability of past climate from a 250-kyr ice-core record. *Nature*, 364:218–220, 1993. doi: 10.1038/364218a0.

[3] Guido Vettoretti and W. Richard Peltier. Fast physics and slow physics in the nonlinear dansgaard–oeschger relaxation oscillation. *Journal of Climate*, 31(9):3423 – 3449, 2018. doi: 10.1175/JCLI-D-17-0559.1. URL `https://journals.ametsoc.org/view/journals/clim/31/9/jcli-d-17-0559.1.xml`.

[4] Carl Wunsch and Patrick Heimbach. Two decades of the atlantic meridional overturning circulation: Anatomy, variations, extremes, prediction, and overcoming its limitations. *Journal of Climate*, 26(18):7167 – 7186, 2013. doi: 10.1175/JCLI-D-12-00478.1. URL `https://journals.ametsoc.org/view/journals/clim/26/18/jcli-d-12-00478.1.xml`.

[5] Brian M. de Silva, Kathleen Champion, Markus Quade, Jean-Christophe Loiseau, J. Nathan Kutz, and Steven L. Brunton. Pysindy: A python package for the sparse identification of nonlinear dynamical systems from data. *Journal of Open Source Software*, 5(49):2104, 2020. doi: 10.21105/joss.02104. URL `https://doi.org/10.21105/joss.02104`.

[6] G. Vettoretti, P. Ditlevsen, M. Jochum, S. O. Rasmussen, et al. Atmospheric co2 control of spontaneous millennial-scale ice age climate oscillations. *Nature Geoscience*, 15:300–306, 2022. doi: 10.1038/s41561-022-00920-7.

[7] Guido Vettoretti. guidov/vettoretti_et_al_2022-ng: Vettoretti_et_al_2022, March 2022. URL `https://doi.org/10.5281/zenodo.6372628`.

[8] Alan V. Oppenheim and Cram. Discrete-time signal processing : Alan v. oppenheim, 3rd edition. 2011. URL `https://api.semanticscholar.org/CorpusID:60631199`.

[9] William Davis and Bruce Buffett. Inferring core processes using stochastic models of the geodynamo. *Geophysical Journal International*, 228(3):1478–1493, 10 2021. ISSN 0956-540X. doi: 10.1093/gji/ggab412. URL `https://doi.org/10.1093/gji/ggab412`.

[10] William Davis and Bruce Buffett. Estimation of drift and diffusion functions from unevenly sampled time-series data. *Phys. Rev. E*, 106:014140, Jul 2022. doi: 10.1103/PhysRevE.106.014140. URL `https://link.aps.org/doi/10.1103/PhysRevE.106.014140`.

[11] David Lamouroux and Klaus Lehnertz. Kernel-based regression of drift and diffusion coefficients of stochastic processes. *Physics Letters A*, 373(39):3507–3512, September 2009. doi: 10.1016/j.physleta.2009.07.073.

[12] David Kleinhans. Estimation of drift and diffusion functions from time series data: A maximum likelihood framework. *Phys. Rev. E*, 85:026705, Feb 2012. doi: 10.1103/PhysRevE.85.026705. URL `https://link.aps.org/doi/10.1103/PhysRevE.85.026705`.

[13] John A Rice. *Mathematical statistics and data analysis*. Brooks/Cole Cengage, Belmont CA, 3rd edition. edition, 2007. ISBN 0495118680.

[14] Miles Cranmer. Interpretable machine learning for science with pysr and symbolicregression.jl, 2023. URL https://arxiv.org/abs/2305.01582.

[15] Nour Makke and Sanjay Chawla. Interpretable scientific discovery with symbolic regression: a review. *Artificial Intelligence Review*, 57(1), January 2024. ISSN 1573-7462. doi: 10.1007/s10462-023-10622-0. URL http://dx.doi.org/10.1007/s10462-023-10622-0.

[16] Andrea Murari, Riccardo Rossi, and Michela Gelfusa. Combining neural computation and genetic programming for observational causality detection and causal modelling. *Artif. Intell. Rev.*, 56(7):6365–6401, November 2022. ISSN 0269-2821. doi: 10.1007/s10462-022-10320-3. URL https://doi.org/10.1007/s10462-022-10320-3.

[17] Athanasios Papoulis. *Probability, random variables, and stochastic processes / Athanasios Papoulis.* McGraw-Hill, New York ;, 3rd ed. edition, 1991. ISBN 0070484775.

[18] Steven L. Brunton and J. Nathan Kutz. *Data-Driven Science and Engineering: Machine Learning, Dynamical Systems, and Control*. Cambridge University Press, 2019.

[19] Robert Tibshirani. Regression shrinkage and selection via the lasso. *Journal of the Royal Statistical Society: Series B (Methodological)*, 58(1):267–288, 12 2018. ISSN 0035-9246. doi: 10.1111/j.2517-6161.1996.tb02080.x. URL https://doi.org/10.1111/j.2517-6161.1996.tb02080.x.

[20] Peter Huybers and William Curry. Links between annual, milankovitch and continuum temperature variability. *Nature*, 441(7091):329–332, 2006. ISSN 0028-0836.

[21] Johannes Lohmann and Peter D. Ditlevsen. A consistent statistical model selection for abrupt glacial climate changes. *Climate dynamics*, 52(11):6411–6426, 2019. ISSN 0930-7575.

[22] Gerhard Heinzel, Albrecht Rüdiger, and R Schilling. Spectrum and spectral density estimation by the discrete fourier transform (dft), including a comprehensive list of window functions and some new flat-top windows. *Max-Planck-Institut für Gravitationsphysik*, 12, 01 2002.

[23] Sze-Bi Hsu. *Ordinary differential equations with applications / Sze-Bi Hsu*. Series on applied mathematics. World Scientific, New Jersey, 2nd edition. edition, 2013. ISBN 978-981-445290-8.

[24] Sheldon M Ross. *A first course in probability*. Pearson custom library. Pearson, Harlow, England, ninth edition. edition, 2014. ISBN 9781292024929.

[25] Patrick H. Worley, Arthur A. Mirin, Anthony P. Craig, Mark A. Taylor, John M. Dennis, and Mariana Vertenstein. Performance of the community earth system model. In *SC '11: Proceedings of 2011 International Conference for High Performance Computing, Networking, Storage and Analysis*, pages 1–11, 2011. doi: 10.1145/2063384.2063457.

[26] Hannah Kleppin, Markus Jochum, Bette Otto-Bliesner, Christine A. Shields, and Stephen Yeager. Stochastic atmospheric forcing as a cause of greenland climate transitions. *Journal of Climate*, 28(19):7741 – 7763, 2015. doi: 10.1175/JCLI-D-14-00728.1. URL https://journals.ametsoc.org/view/journals/clim/28/19/jcli-d-14-00728.1.xml.

# A Technical Appendices and Supplementary Material

## A.1 Connection between deterministic and stochastic representations of the system

Define the temporal evolution of the variable of interest $X(t)$ as governed by a stochastic differential equation (SDE), where $f(X)$ denotes the deterministic drift term, $g(X)$ the diffusion amplitude, and $\Gamma(t)$ a Gaussian white noise process representing random forcing in Eq.(2). The system is therefore stochastic, containing both deterministic and statistical components that jointly control its evolution in time [9–12]. The goal is to quantify both deterministic and stochastic contributions by estimating $f(X)$ and $g(X)$ directly from the time series data.

$$\frac{dX}{dt} = f(X) + g(X)\,\Gamma(t), \tag{2}$$

$$dx = f(x,t)\,dt + G(x,t)\,dw, \tag{3}$$

$$X_{t+1} = X_t + f(X_t)\Delta t + g(X_t)\Delta W_t, \quad \Delta W_t \sim \mathcal{N}(0, \Delta t), \tag{4}$$

$$f(x) \approx \frac{\mathbb{E}[X(t+\Delta t) - X(t) \mid X(t) = x]}{\Delta t}, \tag{5}$$

$$g^2(x) \approx \frac{\mathbb{E}[(X(t+\Delta t) - X(t))^2 \mid X(t) = x]}{\Delta t}, \tag{6}$$

$$X(t) = T(t) + R(t), \tag{7}$$

$$T(t) \approx \text{LocalPolynomialFit}(X(t),\ \text{degree} = d), \tag{8}$$

$$\frac{dT}{dt} \approx f_{\text{det}}(X), \quad \text{Var}(R) \approx g^2_{\text{det}}(X). \tag{9}$$

From Eq.(3) to Eq.(9), the equations describe the transition from the continuous stochastic formulation to its data-driven discrete estimation. The system can be expressed in the standard stochastic form, where $f(x,t)$ denotes the deterministic drift, $G(x,t)$ the diffusion coefficient that controls how noise intensity depends on the system state, and $w(t)$ a standard Wiener process representing random forcing. From this representation, a discrete-time approximation allows estimation of the drift $f(X)$ from the conditional mean of observed increments and the diffusion $g(X)$ from their conditional variance [8]. Uncertainty in these estimates is quantified by bootstrap resampling, producing upper and lower confidence bounds that correspond to the shaded regions in the plots. When the signal is further decomposed into a deterministic trend $T(t)$ and residual fluctuations $R(t)$, the derivative of $T(t)$ represents the deterministic drift $f_{\text{det}}(X)$, and the variance of $R(t)$ corresponds to the deterministic diffusion $g^2_{\text{det}}(X)$.

Smoothing is applied using a 30-year moving-average filter, which suppresses short-term fluctuations while preserving long-term trends, thus clarifies the underlying deterministic structure of the system. The resulting plot quantifies the deterministic and stochastic components of the system, where the drift reflects the mean directional tendency, the diffusion indicates variability strength, and the confidence intervals capture estimation uncertainty across the system states (Figure A.1). We note that in the unsmoothed panels, drift and diffusion estimates show high variability and wide confidence intervals, reflecting strong stochastic fluctuations, while the smoothed panels exhibit reduced diffusion and clearer drift, indicating suppressed short-term noise and preserved large-scale dynamics.

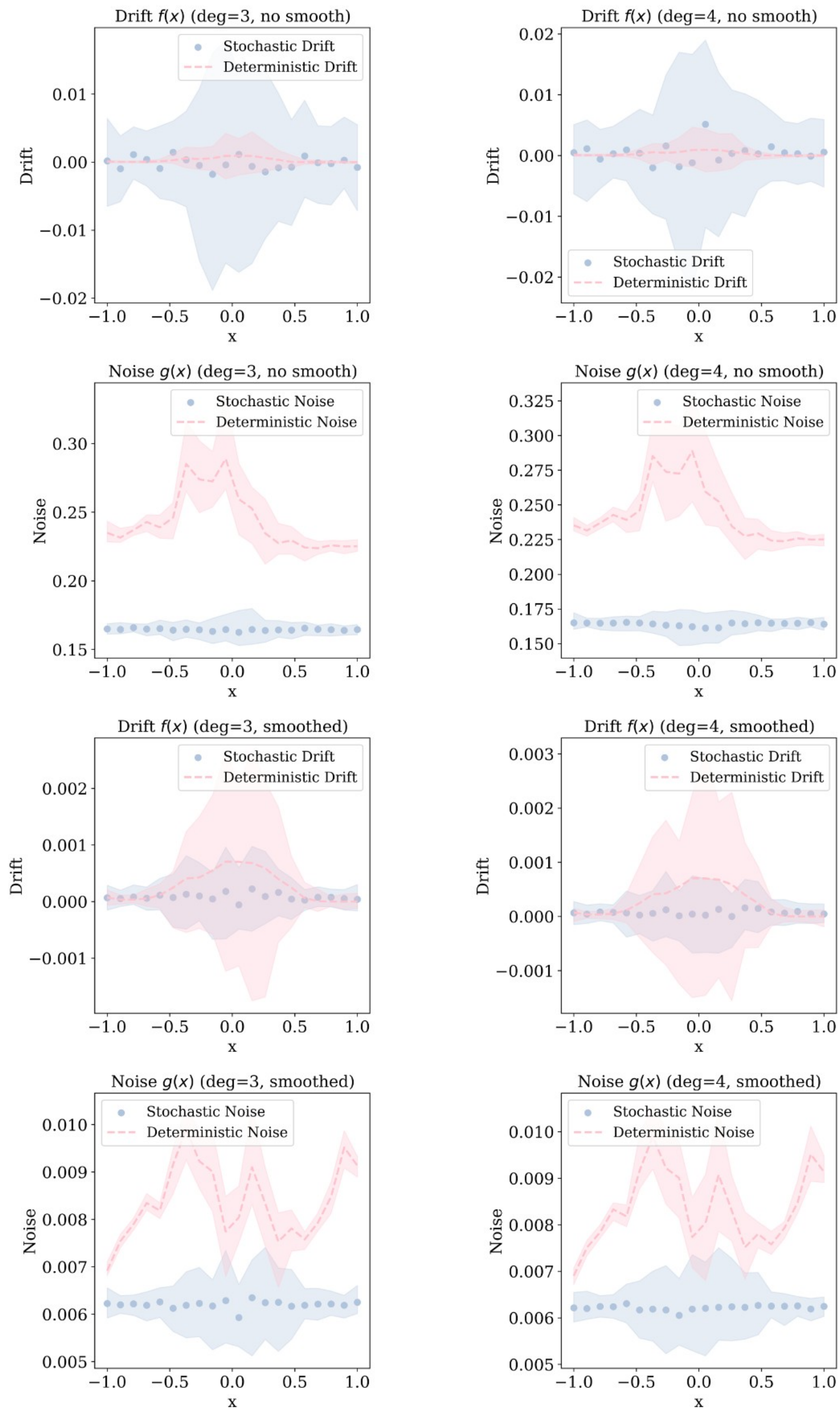


Figure A.1: Estimated drift $f(x)$ and diffusion $g(x)$ functions for unsmoothed and smoothed data using polynomial degrees 3 and 4. The $x$-axis represents the system state $x$, the current value of the variable, and the $y$-axis represents the corresponding drift or diffusion magnitude. Blue points and shading indicate stochastic estimates with bootstrap confidence intervals, whereas pink dashed lines and shading represent deterministic components derived from the smoothed trend.

## A.2 Model Evaluation

As there is not yet a universal way to evaluate a model's out-of-sample extrapolation performance, we compare the errors between the power spectra of the four different CESM simulation runs and our data-driven SDE model simulation. All polynomial and $\ell_1$-regularized polynomial models up to degree 3 and up to degree 4, with and without 30-year smoothing and driven by Gaussian or empirical noise, are evaluated with the CESM AMOC baseline (Fig. A.2). The power Spectra are estimated from normalized Fourier transforms of each time series, averaged over positive frequencies, and plotted as spectral energy density versus frequency on log–log scales to compare continuum variability and scaling behavior [20, 22](Fig. A.3).

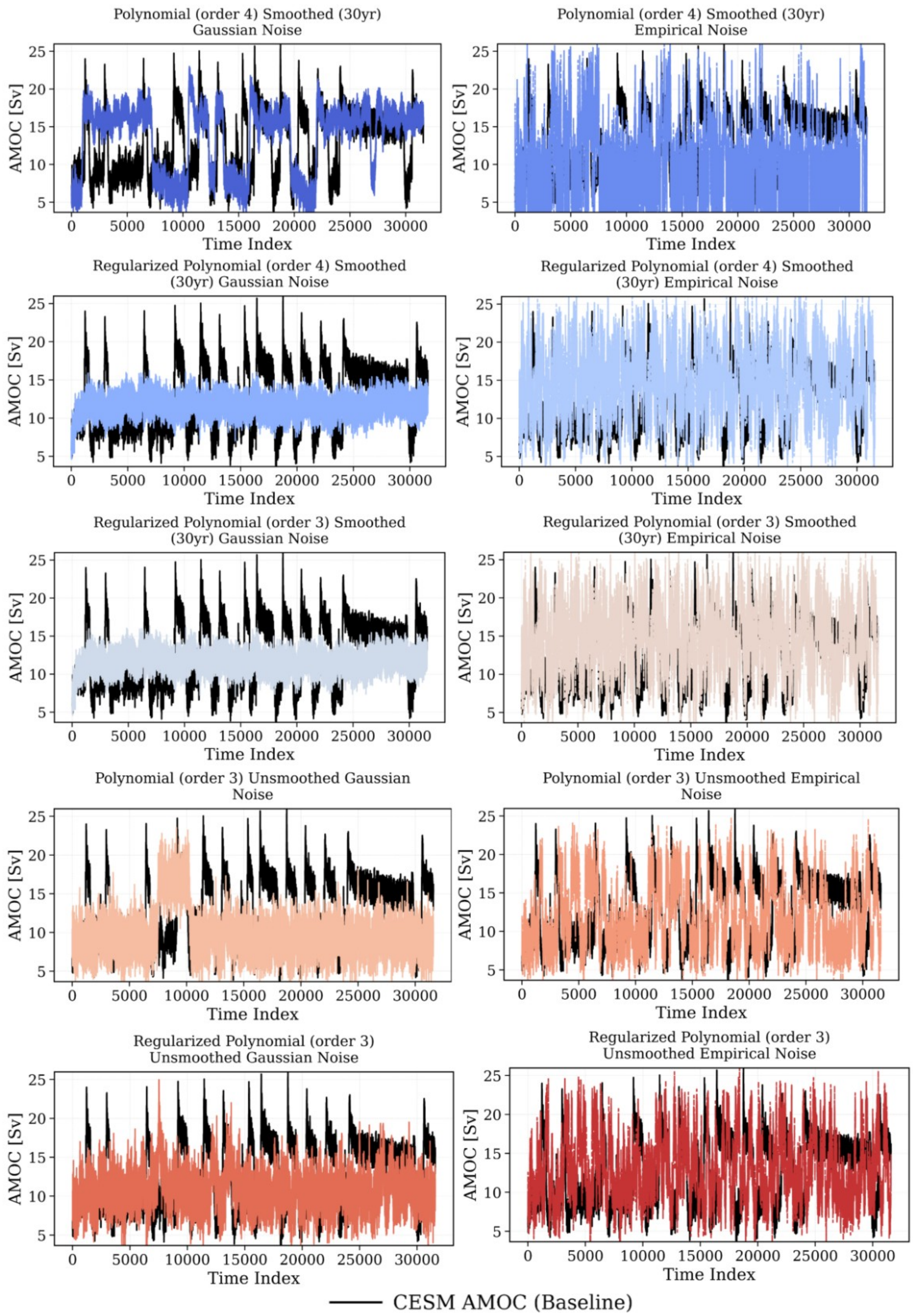


Figure A.2: Comparison between CESM AMOC baseline and all polynomial and $\ell_1$-regularized polynomial models up to degree 3 and up to degree 4, with and without 30-year smoothing and driven by Gaussian or empirical noise.

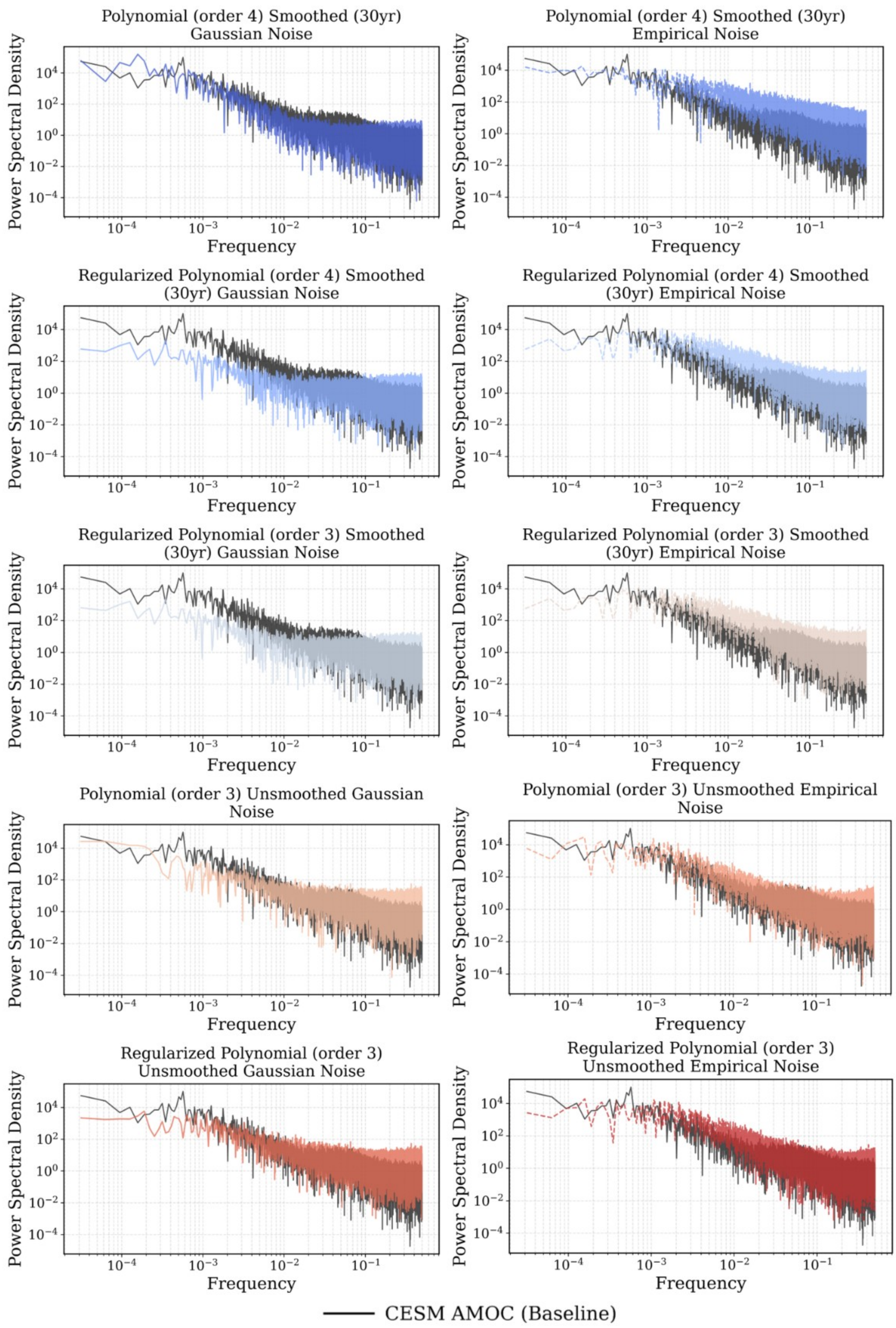


Figure A.3: Power spectra of AMOC segments from four CESM runs and all polynomial and $\ell_1$-regularized polynomial models up to degree 4, showing spectral energy density versus frequency on log–log scales to compare continuum variability and scaling behavior.

$$\hat{X}(f_k) = \sum_{n=0}^{N-1} x_n e^{-2\pi i f_k n/N}, \tag{10}$$

$$P(f_k) = \frac{|\hat{X}(f_k)|^2}{\sum_k |\hat{X}(f_k)|^2}, \tag{11}$$

$$W(P_1, P_2) = \int_0^\infty \big|F_1(f) - F_2(f)\big| df, \tag{12}$$

$$\bar{W} = \frac{1}{N} \sum_{i=1}^{N} W\big(P_{\text{CESM}_i}(f), P_{\text{model}}(f)\big). \tag{13}$$

Spectra are estimated using the discrete Fourier transform to obtain normalized spectral energy density $P(f)$, representing the distribution of variance across frequencies (Eq. 10, Eq.11). The Wasserstein distance $W(P_1, P_2)$ measures the displacement of spectral energy between CESM runs and model spectra (Eq. 12). The mean Wasserstein distance $\bar{W}$ is computed across four CESM segments to evaluate the overall similarity in continuum variability between model simulations and CESM spectral estimates (Eq. 13). Tables A.1–A.3 show spectral pairwise Wasserstein distances between model simulations and CESM segments for the three key variables. We show polynomial model of degree 4 with 30-year smoothing and Gaussian noise best reproduces the transition dynamics observed in the CESM record.

Table A.1: Spectral Pairwise Wasserstein distances between model simulations and CESM segments for AMOC_40N (bold = better than CESM internal variability $< 5.3\text{e} - 5$)

| **Model** | **CESM Run1** | **CESM Run2** | **CESM Run3** | **CESM Run4** |
|---|---|---|---|---|
| Polynomial (deg 4)<br>Smoothed 30 yr, Gaussian Noise | 1.12e-4 | 1.37e-4 | **5.2e-5** | 1.14e-4 |
| Polynomial (deg 4)<br>Smoothed 30 yr, Empirical Noise | 2.33e-4 | 2.59e-4 | 2.69e-4 | 2.23e-4 |
| Regularized Polynomial (deg 4)<br>Smoothed 30 yr, Gaussian Noise | 3.05e-4 | 3.17e-4 | 3.20e-4 | 2.98e-4 |
| Regularized Polynomial (deg 4)<br>Smoothed 30 yr, Empirical Noise | 2.35e-4 | 2.63e-4 | 2.73e-4 | 2.24e-4 |
| Regularized Polynomial (deg 3)<br>Smoothed 30 yr, Gaussian Noise | 3.01e-4 | 3.13e-4 | 3.16e-4 | 2.94e-4 |
| Regularized Polynomial (deg 3)<br>Smoothed 30 yr, Empirical Noise | 2.35e-4 | 2.63e-4 | 2.73e-4 | 2.23e-4 |
| Polynomial (deg 3)<br>Unsmoothed, Gaussian Noise | 2.29e-4 | 1.97e-4 | 1.94e-4 | 2.47e-4 |
| Polynomial (deg 3)<br>Unsmoothed, Empirical Noise | 7.4e-5 | 1.99e-4 | 1.75e-4 | 7.5e-5 |
| Regularized Polynomial (deg 3)<br>Unsmoothed, Gaussian Noise | 2.41e-4 | 2.63e-4 | 2.66e-4 | 2.33e-4 |
| Regularized Polynomial (deg 3)<br>Unsmoothed, Empirical Noise | 1.39e-4 | 2.18e-4 | 2.10e-4 | 1.33e-4 |

Table A.2: Spectral Pairwise Wasserstein distances between model simulations and CESM segments for SFWF (bold = better than CESM internal variability $< 5.4\mathrm{e}-5$)

| **Model** | **CESM Run1** | **CESM Run2** | **CESM Run3** | **CESM Run4** |
|---|---|---|---|---|
| Polynomial (deg 4) Smoothed 30 yr, Gaussian Noise | 1.28e-4 | 1.30e-4 | **4.00e-5** | 1.25e-4 |
| Polynomial (deg 4) Smoothed 30 yr, Empirical Noise | 2.22e-4 | 2.69e-4 | 2.70e-4 | 1.96e-4 |
| Regularized Polynomial (deg 4) Smoothed 30 yr, Gaussian Noise | 2.93e-4 | 3.13e-4 | 3.12e-4 | 2.61e-4 |
| Regularized Polynomial (deg 4) Smoothed 30 yr, Empirical Noise | 2.24e-4 | 2.75e-4 | 2.74e-4 | 1.98e-4 |
| Regularized Polynomial (deg 3) Smoothed 30 yr, Gaussian Noise | 2.89e-4 | 3.10e-4 | 3.08e-4 | 2.57e-4 |
| Regularized Polynomial (deg 3) Smoothed 30 yr, Empirical Noise | 2.24e-4 | 2.75e-4 | 2.74e-4 | 1.97e-4 |
| Polynomial (deg 3) Unsmoothed, Gaussian Noise | 2.41e-4 | 1.99e-4 | 1.86e-4 | 2.09e-4 |
| Polynomial (deg 3) Unsmoothed, Empirical Noise | 6.50e-5 | 2.10e-4 | 1.74e-4 | 8.90e-5 |
| Regularized Polynomial (deg 3) Unsmoothed, Gaussian Noise | 2.32e-4 | 2.69e-4 | 2.66e-4 | 2.03e-4 |
| Regularized Polynomial (deg 3) Unsmoothed, Empirical Noise | 1.34e-4 | 2.30e-4 | 2.09e-4 | 1.41e-4 |

Table A.3: Spectral Pairwise Wasserstein distances between model simulations and CESM segments for PD_200m (bold = better than CESM internal variability $< 7.2\mathrm{e}-5$)

| **Model** | **CESM Run1** | **CESM Run2** | **CESM Run3** | **CESM Run4** |
|---|---|---|---|---|
| Polynomial (deg 4) Smoothed 30 yr, Gaussian Noise | 1.05e-4 | 1.48e-4 | **5.70e-5** | 7.80e-5 |
| Polynomial (deg 4) Smoothed 30 yr, Empirical Noise | 2.70e-4 | 2.89e-4 | 3.09e-4 | 2.80e-4 |
| Regularized Polynomial (deg 4) Smoothed 30 yr, Gaussian Noise | 3.28e-4 | 3.38e-4 | 3.42e-4 | 3.33e-4 |
| Regularized Polynomial (deg 4) Smoothed 30 yr, Empirical Noise | 2.70e-4 | 2.93e-4 | 3.13e-4 | 2.84e-4 |
| Regularized Polynomial (deg 3) Smoothed 30 yr, Gaussian Noise | 3.24e-4 | 3.34e-4 | 3.38e-4 | 3.29e-4 |
| Regularized Polynomial (deg 3) Smoothed 30 yr, Empirical Noise | 2.70e-4 | 2.92e-4 | 3.12e-4 | 2.84e-4 |
| Polynomial (deg 3) Unsmoothed, Gaussian Noise | 2.43e-4 | 2.18e-4 | 2.17e-4 | 2.54e-4 |
| Polynomial (deg 3) Unsmoothed, Empirical Noise | 1.01e-4 | 2.19e-4 | 2.19e-4 | 1.47e-4 |
| Regularized Polynomial (deg 3) Unsmoothed, Gaussian Noise | 2.76e-4 | 2.91e-4 | 3.03e-4 | 2.81e-4 |
| Regularized Polynomial (deg 3) Unsmoothed, Empirical Noise | 1.67e-4 | 2.38e-4 | 2.55e-4 | 2.00e-4 |

The time-reversal asymmetry statistic $M(\tau)$ in Eq. 14 quantifies the saw-tooth shape of Dansgaard-Oeschger (D-O) events in the $\delta^{18}$O record, representing the tendency for rapid warming transitions followed by gradual cooling [21]. Consider a time series $x(t)$, the time-reversal asymmetry can be measured by the skewed difference statistic

$$M(\tau) = \frac{\langle [x(t) - x(t+\tau)]^3 \rangle}{\langle [x(t) - x(t+\tau)]^2 \rangle}, \tag{14}$$

where $\langle \cdot \rangle$ is the expectation value over the time series and $\tau$ represents a characteristic time scale [21]. We note that the polynomial model of degree 4 with 30-year smoothing and Gaussian noise best reproduces the observed time-reversal asymmetry, consistent with the results from the spectral analysis (Figure A.4).

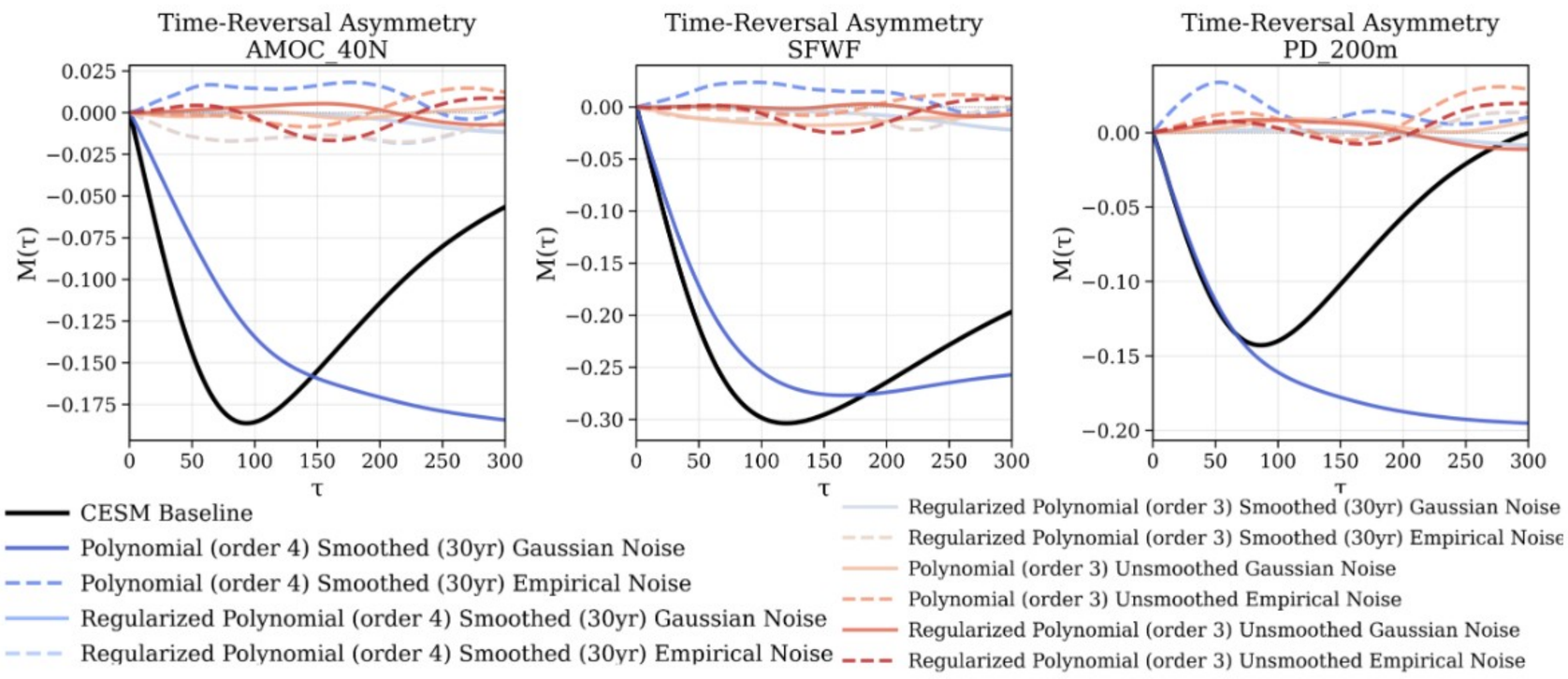


Figure A.4: Time-reversal asymmetry $M(\tau)$ for AMOC_40N, SFWF, and PD_200m, comparing CESM baselines with polynomial and $\ell_1$-regularized polynomial models up to degree 3 and degree 4.

## References

All references cited in the appendix are included in the main reference list.